Light-Induced Reversal of Ion-Segregation in Mixed-Halide Perovskites

Wenxin Mao[1,4†], Christopher R. Hall[2†], Stefano Bernardi[3, 6†], Yi-Bing Cheng[4,5], Asaph Widmer-Cooper[3, 6*], Trevor A. Smith[2*], Udo Bach[1,4*]

[1]*Australian Research Council Centre of Excellence in Exciton Science, Department of Chemical Engineering, Monash University, Clayton, Vic 3800, Australia.*

[2]*Australian Research Council Centre of Excellence in Exciton Science, School of Chemistry, University of Melbourne, Melbourne, Vic 3010, Australia.*

[3]*Australian Research Council Centre of Excellence in Exciton Science, School of Chemistry, University of Sydney, Sydney, NSW 2006, Australia.*

[4]*The Australian Centre for Advanced Photovoltaics (ACAP), Monash University, Victoria 3800, Australia.*

[5]*State Key Laboratory of Advanced Technology for Materials Synthesis and Processing, Wuhan University of Technology, Wuhan 430070, Hubei, China.*

[6]*The University of Sydney Nano Institute, University of Sydney, Sydney, NSW 2006, Australia.*

*Correspondence to: Udo Bach udo.bach@monash.edu; Trevor Smith trevoras@unimelb.edu.au; Asaph Widmer- Cooper asaph.widmer-cooper@sydney.edu.au.

†These authors contributed equally to this work.

Bandgap-instability in mixed-halide perovskites, owing to light-induced phase-segregation, is poorly understood and presents a major challenge for their future commercial use. Here we demonstrate that photoinduced halide-ion segregation can be completely reversed at sufficiently high illumination intensities. With control over halide segregation we tune the optical bandgap of a single mixed-halide perovskite crystal by simply optimizing the input photogenerated carrier density. We develop a polaron-based 2D lattice model that rationalises the experimentally observed phenomena by assuming that the driving force for photoinduced halide segregation is dependent on carrier-induced strain gradients that vanish at high carrier densities. Using illumination sources with different excitation intensities we demonstrate write-read-erase experiments, showing that it is possible to store information in the form of latent images over several minutes. This new ability to control the local halide-ion composition could become key to solving the issue of halide-ion segregation in these materials, and presents new opportunities for their use in concentrator and tandem solar cells, as well as in high-power light-emissive devices and optical memory applications.

Lead halide perovskite (LHP) is a leading semiconductor for a new generation of solar cells, light-emitting devices (LEDs) and photodetectors[1, 2, 3]. A requirement for many optoelectronic applications is the ability to tune the semiconductor bandgap[4, 5]. The bandgap of LHPs can be tuned across the visible and near-infrared regions by controlling the halide ratio, however the stability remains an ongoing issue owing to the soft lattice and high ionic diffusivity[6, 7, 8]. For these mixed halide perovskites, photoinduced halide-ion segregation (PHS) leads to the formation of halide-rich domains and localised variations in material bandgap[9, 10]. This has the effect of reducing device open-circuit voltage, charge mobility, and carrier lifetime, adversely affecting device performance[8, 11].

Several different approaches have been proposed to overcome or limit the effects of PHS. This includes growing larger grains to reduce the influence of grain boundaries, where the phase-segregated domains are found to preferentially form[12, 13]. Recently, approaches based on controlling grain surface-to-volume ratio have indicated a suppression of PHS[14, 15]. Furthermore, passivation of defects, particularly halide vacancies, at grain boundaries, has been shown to suppress ion-migration[15, 16, 17, 18]. While grain boundaries play an important role, point defects are present throughout perovskite crystals and PHS also occurs away from the boundary[13, 19]. The perovskite composition has also been shown to be important. The inclusion of Cs^+ in mixed cation perovskites can inhibit the formation of stable phase-segregated domains[20], while a recent combined Cs^+ mixed cation and triple-halide system exhibits strongly suppressed phase-segregation at high I compositions[18].

Here we demonstrate that photoinduced halide-ion segregation can be actively controlled *in-situ* with light and investigate the driving mechanisms using fluorescence microspectroscopy. We develop a 2D lattice model that reproduces the experimental results by assuming that the driving force for photoinduced phase-segregation is dependent on carrier-induced strain gradients that vanish at sufficiently high carrier densities. The ability to control

ion segregation could become key to solving the issue of halide demixing and to harness the exceptional opportunities associated with a bandgap tuneable semiconductor material. Our work creates a new pathway for the application of mixed-halide perovskites in photovoltaics, including tandem solar cells and concentrator solar cells, and new opportunities in optical switching and memory applications.

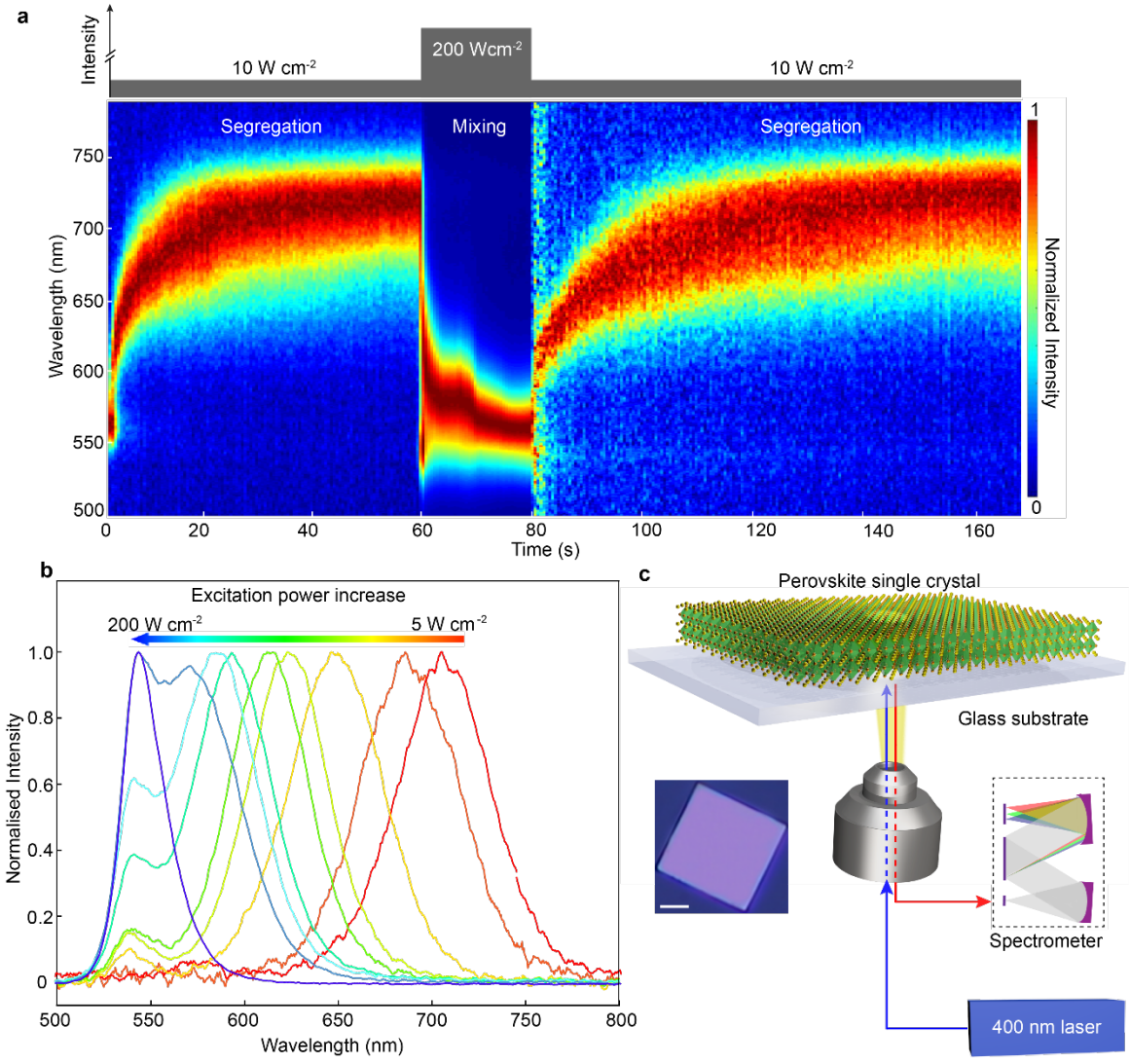


Fig. 1 | Photoinduced halide-ion segregation (PHS) and mixing (PHM) within a $MAPb(Br_{0.8}I_{0.2})_3$ single crystal microplatelet. a, Normalised PL emission spectra recorded upon illumination with a pulsed laser with low excitation intensity (10 W cm^{-2}) over 60 s, followed by high intensity (200 W cm^{-2}) over 20 s, and back to low intensity (10 W cm^{-2}) over 80 s. **b**, Normalised power-dependent PL emission spectra recorded with a range of excitation powers. The arrow indicates the shift in peak position as the excitation power increases. Each steady-state spectrum, recorded at the same crystal position, is reached after 20 s of laser illumination. The excitation

intensity was sequentially increased from 5 to 200 W cm^{-2}. **c**, Schematic of the confocal photoluminescence (PL) microspectroscopy system. Excitation was provided by a 400 nm pulsed laser with a repetition rate of 2.7 MHz. The beam was focused at the centre of the microplatelet in a non-scanning mode. Fluorescence from the illuminated spot was collected and spectrally resolved. The inset shows an optical image of a perovskite microplatelet. The scale bar is 5 μm.

Reversing halide-ion segregation with light

For this study we use single crystal microplatelets to visualise and probe PHS away from grain boundaries. We fabricated single-crystal $MAPb(Br_{0.8}I_{0.2})_3$ microplatelets following our recently reported method[13, 19, 21]. One dimensional (1D) intermediate structure $MAPbBr_{1.37}I_{1.63}$·DMF was fabricated via the antisolvent method at 0 °C. Upon heating to 30 °C on a glass substrate the 1D intermediate melted, producing a supersaturated solution of precursor material from which single-crystalline microplatelets grew. The crystals have an average size of 30 μm and thickness of 0.5-0.8 μm (Supplementary Fig. 1 and 2). The I:Br ratio in the final perovskite crystal is controlled by varying the precursor composition and fabrication temperature[19, 22]. The bandgap increases monotonically as the relative Br composition is increased from 0 to 1[23]. Here the microplatelet growth parameters are selected for an I:Br ratio of 2:8 so the emission from the as-grown material and phase segregated I-rich domains is well separated. The composition of the microplatelets was confirmed with X-ray photoelectron spectroscopy (XPS) (Supplementary Fig. 3).

Using a confocal microscope (Fig. 1c) we recorded photoluminesence (PL) spectra from a fixed position at the centre of a microplatelet. The spot was continuously illuminated with an excitation intensity of 10 W cm^{-2} for 60 s, followed by a 20 s period at 200 W cm^{-2} and a final period of 80 s at 10 W cm^{-2} using a 400 nm pulsed laser, with spectra recorded every 0.5 s. The complete time-dependent spectral information is provided in Fig. 1a. After resting in the dark, upon exposure to low intensity light an emission peak appears at ~550 nm and

slowly red-shifts to ~710 nm over the first 60 seconds. Immediately after the intensity is increased to 200 W cm^{-2}, three emission peaks centred at 545 nm, 610 nm and 710 nm are observed (Supplementary Fig. 15). Over time the peaks at 545 nm and 610 nm red- and blue-shift, respectively, to form a single peak at ~555 nm, whereas the peak at 710 nm decays to zero. When the intensity is reduced to 10 W cm^{-2} for another 80 s the emission peak at 555 nm again red-shifts, reproducing the initial phase-segregated emission (Supplementary Fig. 14). The red-shift over the first 60 s is characteristic of the formation of I-rich domains, and is a clear signature of PHS[19, 24]. PHS readily occurs in polycrystalline films and single-crystals with above bandgap excitation at intensities > 5 mW cm^{-2} [8, 12, 13, 19, 20]. At 200 W cm^{-2}, emission from Br-rich, I-rich and intermediate halide compositions is observed. The decay of the peak at 710 nm and the growth of a high-bandgap peak at 555 nm suggests the I-rich domains decompose and the as-grown low-I composition is restored at high intensity (Supplementary Fig. 15). This is further supported by the red-shift of the Br-rich peak at 545 nm to 555 nm, indicating that a mixed composition material is formed (details for multiple PHM-PHS cycles can be found in Supplementary Fig. 23). By finely tuning the input excitation power (Fig. 1b), a wide range of stabilised PL emission can be reached indicating that the distribution of halide ions is highly correlated with the input excitation power. From here onwards we term this process Photoinduced Halide-ion Mixing (PHM). PHS again takes place when the intensity is reduced. The reversibility of these spectral features shows that the halide ion distribution can be controlled *in-situ* by the excitation intensity. These processes are also observed in a $MAPb(Br_{0.4}I_{0.6})_3$ single crystal (Supplementary Figs. 21, 22). As a comparison, no peak-shift occurs in the pure tri-halide system (Supplementary Fig. 8), suggesting that sample degradation, heating or atmospheric interaction is not responsible for the observed phenomena and that these processes are intrinsic to the mixed halide system. No sample degradation was observed under these experimental conditions (Supplementary Fig. 13). We also note that the

PHM effect presented is reproducible, having been observed on multiple freshly made crystals over a period of 12 months.

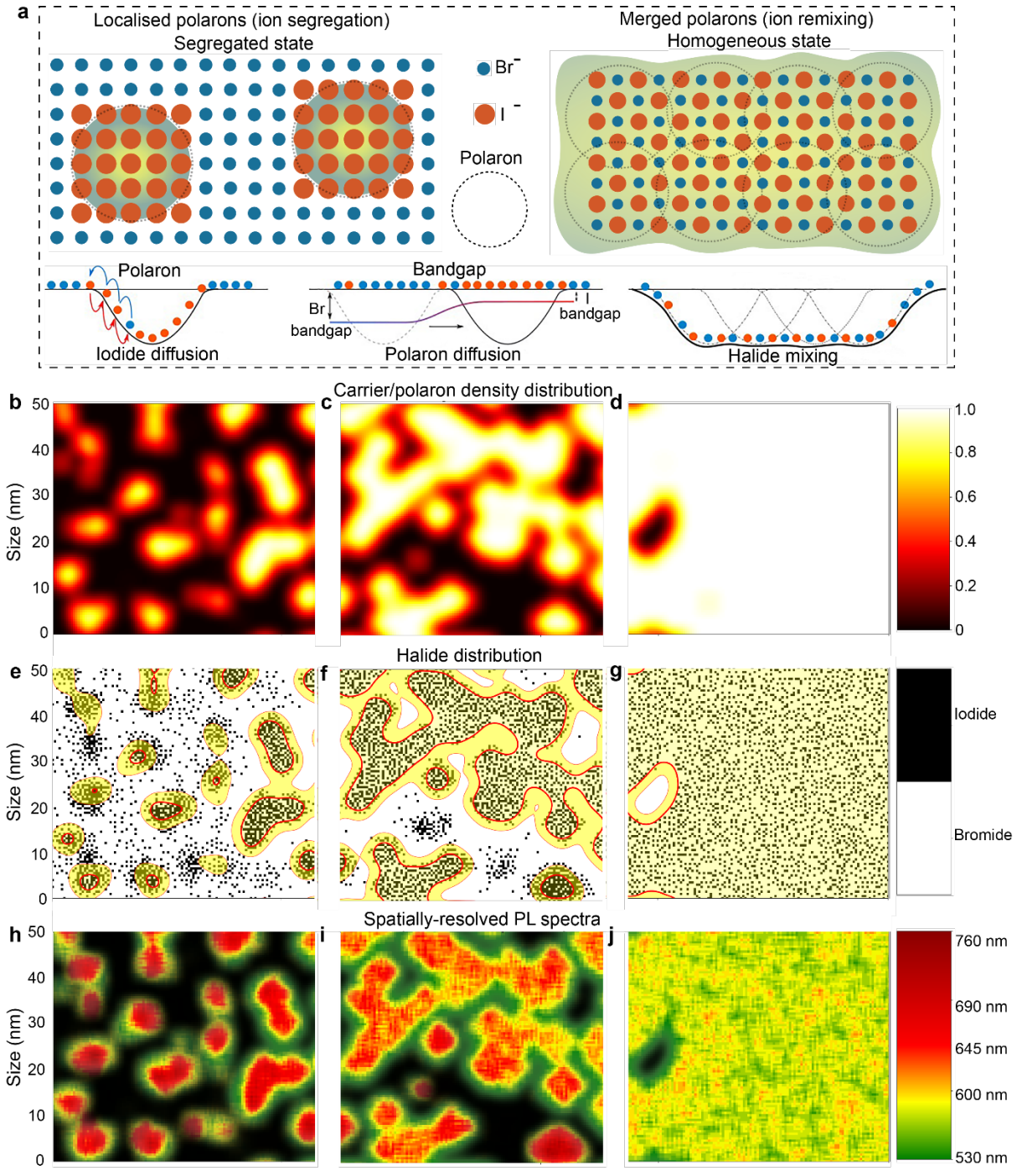


Fig. 2 | Modelling of halide segregation and mixing in response to polaron density (steady state). a, Illustration of halide ion distribution for a $MAPb(Br_{0.8}I_{0.2})_3$ perovskite lattice in response to low carrier density (left) and high carrier density (right). The lattice model includes three driving mechanisms: (i) iodide diffusion along polaron strain gradients; (ii) polaron diffusion along iodide concentration gradients; and (iii) halide mixing

in the absence of strong strain gradients. **b-j**, Simulation results for the lattice model: **b-d**, polaron distributions at different carrier densities (**b**-low, **c**-medium, **d**-high); **e-g**, halide distributions in **b**, **c** and **d**, respectively; **h-j**, corresponding spatially-resolved PL emission peak wavelength. The model shows how the local halide composition and bandgap can be controlled by the carrier density.

Simulations of the halide-ion distribution as a function of photogenerated carrier density

Several mechanisms have been proposed to describe PHS in mixed halide perovskites. Brivio *et al.* [25] proposed a temperature dependent miscibility gap, however, the model does not explain recovery of the mixed phase in the dark, or PHS at low I^- concentrations (<20%). Draguta *et al.*[26] identified an anti-entropic driving force for segregation in the energy gap between homogeneous and segregated I-rich regions, however the sign of the driving force seems independent of the photoexcitation power and of the spatial extent of the region being excited. Bischak *et al.*[13] argued that PHS is due to the formation of polarons, i.e. deformation of the ionic perovskite lattice in the vicinity of charge carriers. In their analysis, the change in the lattice spacing near photoexcited charge carriers provides the driving force for halides of different species to segregate.

None of these models describe PHM observed under high photon flux, at least not in their current form. Instead, we have developed a lattice model, which builds on the concept of polaron induced segregation, to model changes in halide distribution in response to a wide range of illumination powers. The model considers three driving forces: (i) a force which locally attracts iodides towards polarons due to the strain gradients which they generate, (ii) a force which attracts carriers/polarons towards iodide rich regions due to the reduction (or funnel) in the bandgap, and (iii) a force which drives the halides to mix homogeneously in the absence of strong strain gradients (see Fig. 2a). With this physical picture, and a reasonable limit on how strongly polarons can overlap (see Model – Further Discussion in the

Supplementary Material), remixing will naturally occur under strong illumination due to the reduction in strain gradient where the polarons overlap or merge.

The model is based on the Kawasaki Hamiltonian with local exchange.

$$H = -J\Sigma_{(i,j)^{2nd}}\sigma_i\sigma_j - \Sigma_i h_i\sigma_i$$

Halide ions are represented as nodes (*i, j*) on a 2D lattice that can exchange position with neighbouring ions, with the time evolution solved using a Monte Carlo (MC) algorithm. The tendency of halides to mix in the dark or in the absence of strain gradients is described by the first term of the Hamiltonian, in which J represents the interaction energy between neighbouring ions, which in our case favours mixing. The interaction with light induced polarons is described by the second term, where the energy h_i defines the coupling strength between a halide at a particular node and a polaron present at that location. The difference between h_i at adjacent sites represents the gradient in strain that the polarons generate on the perovskite framework and is the driving force for segregation. The polarons are modeled as gaussian distributions with standard deviation $\sigma \sim 3$ lattice sites[27, 28, 29], and their effect is to locally alter the halide composition by favoring exchanges in which iodide ions diffuse within the area delimited by the polaron. Where polarons overlap, however, the strain gradient is reduced and the driving force for segregation disappears. Note that in this work we do not distinguish between electrons and holes as quantitative agreement on their effects on the ionic framework (e.g. lattice relaxations and distortions) is still lacking[28, 30, 31, 32].

The halide distribution, in turn, determines the local bandgap and biases the location of the polarons at each MC cycle, which we treat as statistically independent due to the vast difference in timescales between charge carrier and halide dynamics[29, 33]. Due to the bandgap funnelling effect[34], regions of high iodide concentration, having a smaller bandgap, act as traps for carriers. This causes carriers to diffuse towards these areas and preferentially recombine there. While the exact shape of this bias is unknown, our results are robust to variations from

linear to sigmoidal at low iodide concentration (Supplementary Fig. 20). As we were mostly interested in the steady state, only time-independent carrier densities were considered. Full details of the model and simulation parameters can be found in the Methods section, including a discussion of their connection to experimental data.

This model qualitatively accounts for all phenomena observed from low to high excitation intensities and rationalises the change in halide distribution (in both time and space) in terms of the local polaron density. The key results for different excitation regimes, after the model has reached a steady-state, are presented in Fig. 2b-d. This shows the polaron density for low, medium and high photon flux, respectively, with higher density indicated by brighter regions. As the photon flux is increased from low to high, the polaron features increase in size, and start to merge, until a near continuum is observed. The extent and shape of these domains is due to the local density of carriers and the underlying halide distribution. The positions of the I^- and Br^- are shown in Fig. 2e-g, providing insight into the coupling between the polaron and halide distributions. At low and medium photon flux, I^- ions segregate in areas with isolated polarons, while, at the same time, areas with high I^- concentration attract carriers due to the funnelling effect of the local bandgap. This feedback mechanism is consistent with phase-segregated domains self-stabilising under illumination.

In contrast, at sufficiently high photon flux, a wide area can become saturated with polarons. In this region the lattice is uniformly deformed and the driving force for segregation, i.e. the strain gradient, disappears. Entropy now dominates, and the halides become homogeneously distributed across the excited region (Fig. 2g and j). This has the effect of increasing the material bandgap and emission energy which approaches that expected for the given halide stoichiometry. This can be more clearly seen from the predicted spatially-resolved PL spectra, which show: (Fig. 2h) phase segregated I-rich emission (>620nm, red colour) in regions with isolated polarons; (Fig. 2i) intermediate wavelengths in regions where polarons

start to merge; and (Fig. 2j) uniform green emission (~570 nm) in areas that are saturated with polarons. The general picture that emerges is summarized in Fig. 2a.

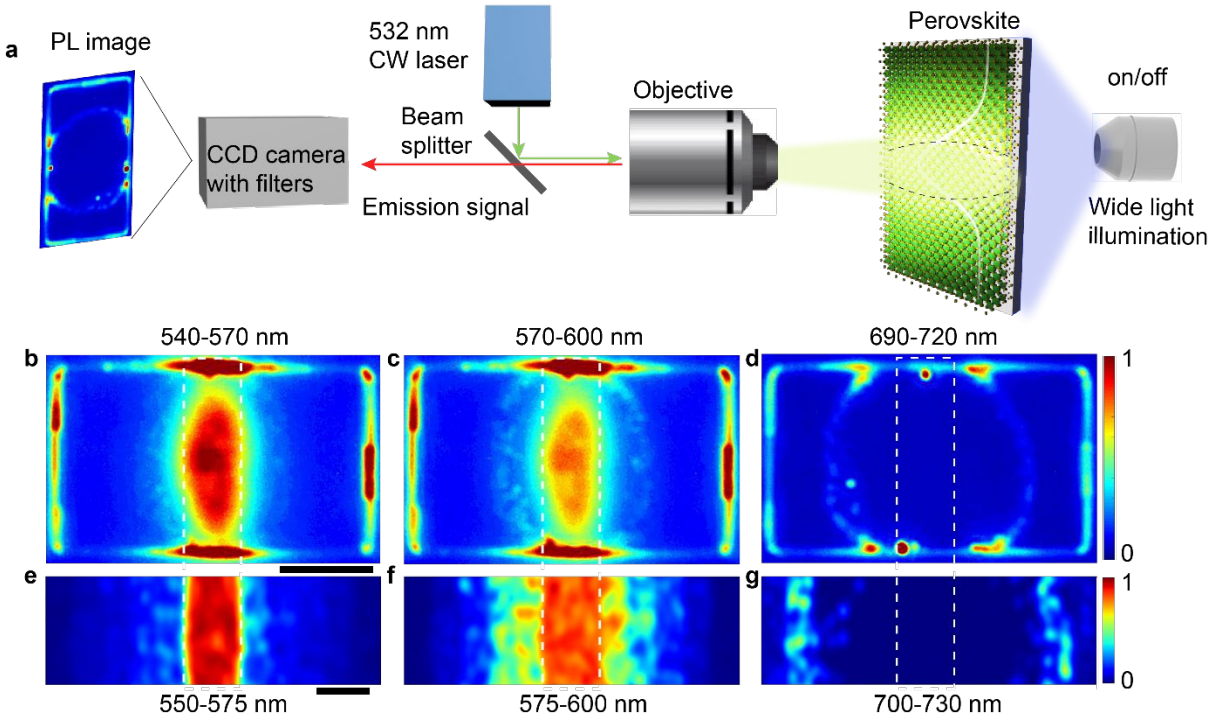


Fig. 3 | Spatially-resolved steady-state PL maps in response to a carrier density gradient. a, Schematic of experimental setup with a $MAPb(Br_{0.8}I_{0.2})_3$ microplatelet under localised excitation by a 532 nm continuous wave (CW) laser with an elliptical beam profile and intensity of 10 W cm^{-2}. A weak filtered (400–450 nm, 5 mW cm^{-2}) light source illuminated the sample from the back to drive phase segregation before the 532 nm laser was switched on. **b-d**, Spatially-resolved (steady state) widefield microscopic PL maps under illumination of the CW laser, collected in three different emission wavelength ranges as specified. Scale bar is 5 µm. **e-g**, PL intensity maps predicted by our lattice model in response to a carrier/polaron gradient. Scale bar is 0.25 µm.

To further examine if the lattice model can reasonably predict the intensity dependent behaviour, we compare the model to an experimentally imposed carrier gradient probed with widefield PL microscopy as shown in Fig. 3a. A large (3.5×8 µm) elliptical excitation spot with a gaussian intensity profile is projected onto the centre of a single microplatelet, with the PL image recorded by a CCD camera coupled to a tuneable bandpass filter. In Fig. 3b-d we show

PL images from a $MAPb(Br_{0.8}I_{0.2})_3$ crystal at three wavelength regions: 540-570 nm, 570-600 nm and 690-720 nm. The measurements were performed with a 532 nm CW laser, which requires a lower intensity (10 W cm^{-2}) to induce PHM than the pulsed laser used in Fig. 1 (higher instantaneous excitation power is required for pulsed excitation due to a combination of carrier relaxation between each pulse[35, 36] and Auger recombination at high carrier densities see Supplementary Fig. 24 for further discussion). The area illuminated by the CW laser shows strong emission in the 540-570 nm window, suggesting efficient PHM in this region. As the narrowband filter is tuned to longer wavelengths, the central emission feature fades while a bright ring appears around the excitation spot. All PL images from 540-720 nm are given in Supplementary Fig. 4. Fig. 3e-g shows the simulated PL intensity maps.

To mimic the action of the focused green CW laser, a polaron density gradient that follows a 1D gaussian distribution centred in the middle and decaying to a low value at the edges is applied to the lattice model. In this case the model predicts PHM at the centre of the platelet and PHS at its edges. It is notable that the appearance of a ring-shaped area with red-shifted emission is well reproduced by the model, which predicts localised partial halide segregation that takes place at intermediate polaron density (Supplementary Fig. 5 provides a more detailed view of the halide distribution weighted by carrier density gradient). The localised changes in halide composition can also be imaged in real time, reaching a steady-state within tens of seconds (Supplementary Fig. 6-7).

It is reasonable to consider that heating induced by the excitation laser may increase the crystal temperature above the miscibility temperature, which conceivably could also reverse halide phase-segregation. To eliminate this possibility, we performed low intensity PL measurements on $MAPb(Br_{0.8}I_{0.2})_3$ microplatelets at both room temperature and at 70°C (Supplementary Fig. 17). In both cases the PL red-shifted, indicating the elevated temperature was unable to drive remixing. We note that this is consistent with the work of Kamat *et al.*[37].

They showed that, while the halide PHS kinetics have an Arrhenius temperature dependence, light-induced halide segregation is not suppressed at temperatures up to 100 °C for excitation intensities above 20 mW cm^{-2}. Since degradation of MHPs occur around 120 °C, this excludes temperature as being the driving mechanism for remixing. Consistent with this, eliminating the temperature gradient in our model yields the same halide distribution in the steady state (Supplementary Fig. 19).

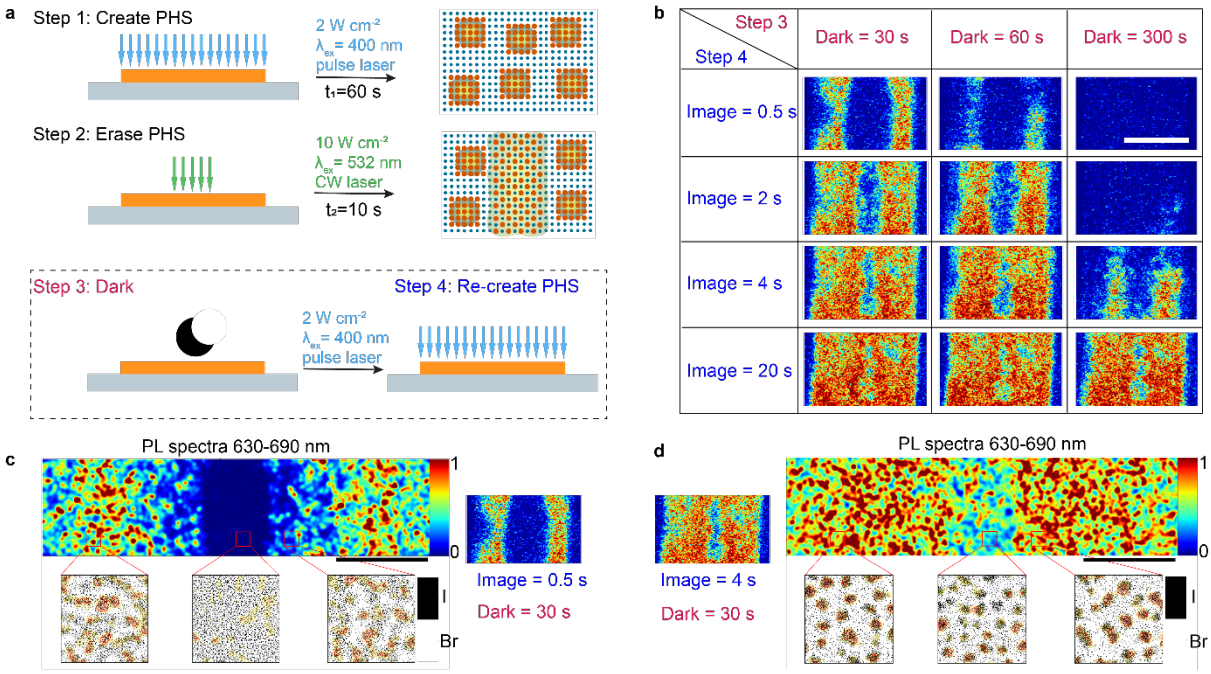


Fig. 4 | Imaging the stability of the mixed-state (PHM) after localised illumination. a, Timeline showing the measurement sequence. A microplatelet was illuminated for 60 s with the excitation beam of a scanning confocal microscope (2 W cm^{-2}, 400 nm pulsed laser) to induce PHS across the crystal, then exposed for 10 s to a focused green laser (10 W cm^{-2} 532 nm CW) to induce PHM at the crystal centre. After a specific time in the dark (30-300 s), the microplatelet was again scanned by a confocal microscope excitation beam to induce halide segregation (PHS). **b**, Images exploring the stability of the spatially encoded PHM feature over time. Time-dependent confocal images of PHS emission (610-700 nm) are shown for three different PHS-PHM-PHS cycles, after waiting times in the dark of 30 s, 60 s, and 300 s, respectively. Scale bar is 5µm. **c-d**, Simulation results corresponding to **b**, where **c** and **d** represent scanning laser times of ~0.5 s and ~4 s, respectively. The insets show the iodide distribution (in black) together with the polaron field isolines in different parts of the crystal.

Localised writing, reading and erasing of phase-segregation

The ability to spatially modify the bandgap of a material may be useful if the process can be reversed in a controlled way. Next we demonstrate that two lasers can be used to create and erase PHS features on a single LHP microplatelet. For this we use a scanning confocal microscope (pulsed, 400 nm, 2 W cm^{-2}, 2.7 MHz) to drive PHS and image emission in the 610-700 nm region. A second laser (CW, 532 nm, 10 W cm^{-2}) is used to induce PHM in the centre of the microplatelet. A schematic outlining the procedure is given in Fig. 4a. Starting with a microplatelet that has rested in the dark, the 400 nm laser is scanned across the sample over 60 s to generate uniform PHS over the entire crystal. At 60 s the 532 nm laser is then switched on for 10 s to write a localized PHM feature, after which the sample is left to rest in the dark for different periods of time. After resting in the dark, the 400 nm scanning beam is switched back on to drive and image the recovery of PHS across the sample, with an image recorded every 0.5 s. The confocal PL images are shown in Fig. 4b, with image sequences recorded after 30 s, 60 s and 300 s in the dark. After 30 s in the dark, a central dark region is initially observed (0.5 s), surrounded by emission from PHS domains. The dark feature fades rapidly over 4 s and is almost gone after 20 s. We attribute the dark feature to PHM generated by the 532 nm laser, with emission falling outside the detected spectral window. A simultaneous measurement of PHS and PHM emission (Supplementary Fig. 9) confirms this interpretation. The PHM region fades from the edges inwards, reflecting the smaller changes required at the edge of the composition gradient observed in Fig. 3b. The bandgap gradient likely pushes charge-carriers away from the PHM region towards the edges where they accumulate, driving halide segregation. The PHM feature is observed for waiting times of up to 300 s. The stability of this state in the dark reinforces that this is the naturally occurring state of the material in the absence

of illumination. The 300 s limit is imposed by the dark induced relaxation of PHS of the surrounding microplatelet. For increasing waiting time, the entire crystal remixed and the spatially defined PHM feature disappears.

Fig. 4c-d shows that the process is also well-described by the lattice model. The simulated remixing of halide-ions in the dark is shown in Supplementary Fig. 10. When exposed to light following a short period in the dark, the model predicts halides at the centre of the lattice remain well-mixed while those towards the sides remain segregated (Fig. 4c). Due to the bandgap gradient across the sample, carriers migrate towards segregated domains (Supplementary Fig. 11). Consequently, as time progresses, halide segregation takes place at the edge of the mixed region and only gradually spreads towards the centre (Fig. 4d), as was observed in 4b. It is notable that no significant evolution takes place beyond Fig. 4d, leaving a small mixed region in the centre. A similar feature is also evident in the experimental data (Fig. 4b, Dark=300 s). The model suggests that the funnelling of carriers away from the mixed centre plays an important role at this final stage of PHS. The dynamic recovery of the segregated state can be further imaged with widefield microscopy (Supplementary Fig. 12), which shows a bright ring of I-rich domains gradually shifting towards the centre of the crystal.

Similar PHS and PHM results are expected for a wide range of Br:I halide ratios (see Fig S18 for modelling results). For high iodide concentrations however, the system is already in a "quasi-segregated" state and little PHS can occur. As shown by Topwal *et al.*[38], at iodide concentrations above 70%, PHS only takes place at low temperatures. At these concentrations, the bandgap landscape is characterised by shallow minima, and only extremely low temperatures can trap and stabilise carriers in segregated domains. This is also evident from the data shown in Supplementary Fig. 18, where the power at which percolation (and later

PHM) occurs decreases at higher I:Br ratios, even though the patterns that the I rich domains form before PHM remain qualitatively similar.

Outlook

The ability to manipulate the halide ion distribution in perovskites with light presents a viable method for achieving compositional uniformity in mixed-halide perovskites. We have provided evidence that the halide-ion distribution in mixed halide perovskite single crystals can be tuned from a segregated state to a completely homogeneous state by increasing the input carrier density; and we have developed a lattice model that explains this behaviour by the presence (or not) of polaron-induced strain gradients. Both the experimental and theoretical results indicate that the PHS can be actively switched on and off by manipulating the carrier/polaron density. This provides a pathway for realizing the full potential of mixed-halide perovskites, including in concentrator and tandem solar cells designs that have the potential to boost efficiencies beyond the Shockley-Queisser limit[39, 40]. In addition, we have shown that it is possible to perform write-read-erase operations on mixed-halide perovskites, which presents new opportunities for the use of perovskites in optical switching and memory applications.

References

1 Stranks, S. D. & Snaith, H. J. Metal-halide perovskites for photovoltaic and light-emitting devices. *Nat. Nanotechnol* **10,** *391 (2015)*.

2 Saliba, M., Correa-Baena, J.-P., Grätzel, M., Hagfeldt, A. & Abate, A. Perovskite solar cells: from the atomic level to film quality and device performance. *Angew. Chem. Int. Ed.* **57,** 2554-2569 (2018)

3 Kojima, A., Teshima, K., Shirai, Y. & Miyasaka, T. Organometal halide perovskites as visible-light sensitizers for photovoltaic cells. *J. Am. Chem. Soc.* **131,** 6050-6051 (2009).

4 Fu, Y. *et al.* Metal halide perovskite nanostructures for optoelectronic applications and the study of physical properties. *Nat. Rev. Mater.* **4,** 169-188 (2019).

5 McMeekin, D. P. *et al.* A mixed-cation lead mixed-halide perovskite absorber for tandem solar cells. *Science* **351**, 151-155 (2016).

6 Azpiroz, J. M., Mosconi, E., Bisquert, J. & De Angelis, F. Defect migration in methylammonium lead iodide and its role in perovskite solar cell operation. *Energy Environ. Sci.* **8**, 2118-2127 (2015).

7 Eames, C. *et al.* Ionic transport in hybrid lead iodide perovskite solar cells. *Nat. Commun* **6**, 7497 (2015).

8 Hoke, E. T. *et al.* Reversible photo-induced trap formation in mixed-halide hybrid perovskites for photovoltaics. *Chem. Sci.* **6**, 613-617 (2015).

9 Eperon, G. E., Hörantner, M. T. & Snaith, H. J. Metal halide perovskite tandem and multiple-junction photovoltaics. *Nat. Rev. Chem.* **1**, 0095 (2017).

10 Leijtens, T., Bush, K. A., Prasanna, R. & McGehee, M. D. Opportunities and challenges for tandem solar cells using metal halide perovskite semiconductors. *Nat. Energy* **3**, 828-838 (2018).

11 Balakrishna R. G., Kobosko S. M., Kamat P. V. Mixed halide perovskite solar cells. Consequence of iodide treatment on phase segregation recovery. *ACS Energy Lett.* **3**, 2267-2272 (2018).

12 Tang, X. *et al.* Local Observation of phase segregation in mixed-halide perovskite. *Nano Lett.* **18**, 2172-2178 (2018).

13 Bischak, C. G. *et al.* Origin of reversible photoinduced phase separation in hybrid perovskites. *Nano Lett.* **17**, 1028-1033 (2017).

14 Gualdrón-Reyes, A. F. *et al.* Controlling the phase segregation in mixed halide perovskites through nanocrystal size. *ACS Energy Lett.* **4**, 54-62 (2019).

15 Wang, X. *et al.* Suppressed phase separation of mixed-halide perovskites confined in endotaxial matrices. *Nat. Commun* **10**, 695 (2019).

16 Kubicki, D. J. *et al.* Phase segregation in potassium-doped lead halide perovskites from 39K solid-state NMR at 21.1 T. *J. Am. Chem. Soc.* **140**, 7232-7238 (2018).

17 Abdi-Jalebi M. *et al.* Maximizing and stabilizing luminescence from halide perovskites with potassium passivation. *Nature* **555**, 497-501 (2018).

18 Xu, J., *et al.* Triple-halide wide–band gap perovskites with suppressed phase segregation for efficient tandems. *Science* **367**, 1097-1104 (2020).

19 Mao, W. *et al.* Visualizing phase segregation in mixed-halide perovskite single crystals. *Angew. Chem. Int. Ed.* **58**, 2893-2898 (2019).

20 Bischak, C. G. *et al.* Tunable polaron distortions control the extent of halide Demixing in lead halide perovskites. *J. Phys. Chem. Lett.* **9**, 3998-4005 (2018).

21 Mao, W. *et al.* Controlled growth of monocrystalline organo-lead halide perovskite and its application in photonic devices. *Angew. Chem. Int. Ed.* **56**, 12486-12491 (2017).

22 Wang, L. *et al.* Tunable bandgap in hybrid perovskite $CH_3NH_3Pb(Br_{3-y}X_y)$ single crystals and photodetector applications. *AIP Adv.* **6**, 045115 (2016).

23 Brennan, M. C., Draguta, S., Kamat, P. V. & Kuno, M. Light-induced anion phase segregation in mixed halide perovskites. *ACS Energy Lett.* **3**, 204-213 (2018).

24 Barker, A. J. *et al.* Defect-assisted photoinduced halide segregation in mixed-halide perovskite thin films. *ACS Energy Lett.* **2**, 1416-1424 (2017).

25 Brivio, F., Caetano, C. & Walsh, A. Thermodynamic origin of photoinstability in the $CH_3NH_3Pb(I_{1-x}Br_x)_3$ hybrid halide perovskite alloy. *J. Phys. Chem. Lett.* **7**, 1083-1087 (2016).

26 Draguta, S. *et al.* Rationalizing the light-induced phase separation of mixed halide organic–inorganic perovskites. *Nat. Commun* **8**, 200 (2017).

27 Ma, J. & Wang, L-W. Nanoscale charge localization induced by random orientations of organic molecules in hybrid perovskite $CH_3NH_3PbI_3$. *Nano Lett.* **15**, 248-253 (2015).

28 Miyata, K. *et al.* Large polarons in lead halide perovskites. *Sci. Adv*. **3**, e1701217 (2017).

29 Zheng, F. & Wang, L-W. Large polaron formation and its effect on electron transport in hybrid perovskites. *Energy Environ. Sci.* **12**, 1219-1230 (2019).

30 Ambrosio, F., Wiktor, J., De Angelis, F. & Pasquarello, A. Origin of low electron–hole recombination rate in metal halide perovskites. *Energy Environ. Sci.* **11**, 101-105 (2018).

31 Uratani, H., Chou, C-P. & Nakai, H. Quantum mechanical molecular dynamics simulations of polaron formation in methylammonium lead iodide perovskite. *Phys. Chem. Chem. Phys*. **22**, 97-106 (2020).

32 Zhou, L. *et al.* Cation alloying delocalizes polarons in lead halide perovskites. *J. Phys. Chem. Lett.* **10**, 3516-3524 (2019).

33 Frost, J. M. & Walsh, A. What is moving in hybrid halide perovskite solar cells? *Acc. Chem.***49**, 528-535 (2016).

34 Noh, J. H., Im, S. H., Heo, J. H., Mandal, T. N. & Seok, S. I. Chemical management for colorful, efficient, and stable inorganic–organic hybrid nanostructured solar cells. *Nano Lett.* **13**, 1764-1769 (2013).

35 Knight, A. J. *et al.* Electronic traps and phase segregation in lead mixed-halide perovskite. *ACS Energy Lett.* **4**, 75-84 (2019).

36 Yang, X. *et al.* Light induced metastable modification of optical properties in $CH_3NH_3PbI_{3-x}Br_x$ perovskite films: two-step mechanism. *Org. Electron.* **34**, 79-83 (2016).

37 Elmelund, T., Seger, B., Kuno, M., Kamat, P. V. How interplay between photo and thermal activation dictates halide ion segregation in mixed halide perovskites. *ACS Energy Lett.* **5**, 56-63 (2020).

38 Nandi, P. *et al.* Temperature dependent photoinduced reversible phase separation in mixed-halide perovskite. *ACS Appl. Energy Mater.* **1**, 3807-3814 (2018).

39 Wang, Z. *et al.* High irradiance performance of metal halide perovskites for concentrator photovoltaics. *Nat. Energy* **3**, 855-861 (2018).

40 Lin, Q., Wang, Z., Snaith, H. J., Johnston, M. B. & Herz, L. M. Hybrid perovskites: prospects for concentrator solar cells. *Adv. Sci.* **5**, 1700792 (2018).

Acknowledgments This work was financially supported by the Australian Research Council through the Centre of Excellence in Exciton Science (CE170100026) and additional grants (DP160104575, LE170100235). We gratefully acknowledge financial support from the Australian Government through the Australian Renewable Energy Agency and the Australian Centre for Advanced Photovoltaics (ACAP). W.M. acknowledges the ACAP fellowship supported by the Australian Government through the Australian Renewable Energy Agency (ARENA). The authors acknowledge the XPS measurement by Dr. Thomas Gengenbach from The Commonwealth Scientific and Industrial Research Organisation (CSIRO). The authors also acknowledge use of facilities within the Monash Centre for Electron Microscopy (MCEM), Monash X-Ray Platform and Melbourne Centre for Nanofabrication (MCN) in the Victorian Noe of the Australian National Fabrication Facility (ANFF). This work was supported by resources provided by the Pawsey Supercomputing Centre with funding from the Australian Government and the Government of Western Australia.

Author contributions U.B., T.A.S. and A.W.-C. conceived the idea and supervised the research. W.M. fabricated and characterized the perovskite microplatelets. C.R.H. and W.M. performed the experiments. S.B. developed and ran the simulations. W.M., C.R.H., S.B., T.A.S., U.B. and A.W.-C. interpreted the data. All authors contributed to writing and reviewing the manuscript.

Competing interests The authors declare no competing interests.

METHODS

Materials. Dimethylformamide (DMF) (99.8%), lead (II) bromide ($PbBr_2$) (99.999%), and diethyl ether (99.9%) were purchased from Sigma-Aldrich. Methylammonium bromide (MABr) (>99%) and methylammonium iodide (MAI) (>99%) were purchased from Dyesol. All chemicals were used without further purification.

Fabrication of perovskite single crystals. The tri-halide ($MAPbBr_3$) and mixed halide ($MAPb(Br_xI_{1-x})_3$) perovskite microplatelets are fabricated following our reported methods[19, 21]. Briefly, $MAPbBr_3$ precursor solution was prepared by dissolving 134.4 mg MABr and 440.4 mg $PbBr_2$ in 1.5 ml anhydrous DMF in a 20 ml vial. Similarly, $MAPb(Br_xI_{1-x})_3$ solution was prepared by dissolving 13.44 mg MABr, 171.72 mg MAI, and 440.4 mg $PbBr_2$ in 1.5 ml DMF for the fabrication of $MAPb(Br_{0.8}I_{0.2})_3$ single crystals and dissolving 190.8 mg MAI and 440.4 mg $PbBr_2$ in 1.5 ml DMF for the fabrication of $MAPb(Br_{0.4}I_{0.6})_3$ single crystals. The precursor solution was placed in a larger vial containing diethyl ether as antisolvent vapour. After storing the above setup at 0 °C for 24 h, white needle-like crystals ($MAPbBr_3$·DMF and $MAPbBr_{1.37}I_{1.63}$·DMF) form in the precursor solution. These precursor crystals were placed on a microscope cover-slip at room temperature, where they melted, providing a supersaturated solution from which $MAPbBr_3$ and $MAPb(Br_xI_{1-x})_3$ microplatelets grew. For the fabrication of the $MAPb(Br_{0.4}I_{0.6})_3$ single crystals, a drop of precursor solution on the cover-slip was pre-heated to 60 °C. The intermediate fibre was then placed in the solution and quickly covered with another glass slide to avoid fast solvent evaporation. The set up was followed by heating up to 80 °C for 2 h to allow the crystal growth. The crystal growth was monitored through a microscope and terminated once crystals of a suitable size were formed. Growth was terminated by removal of the growth solution with a paper tissue.

Scanning electron microscopy (SEM) and Energy-dispersive X-ray spectroscopy (EDS). SEM and EDS images were taken on a FEI Nova NanoSEM 450 FEGSEM. The SEM images were taken at room temperature.

Atomic force microscopy (AFM). AFM measurements were conducted using a Bruker Icon AFM. All measurements were performed in the standard tapping mode with OTESPA-R3 tips from Bruker.

X-ray photoelectron spectroscopic (XPS). XPS analysis was performed with an AXIS Ultra DLD spectrometer (Kratos Analytical, Inc.) at a pressure of around 1×10^{-8} mbar. The measurements were performed with a monochromatic Al-K_α X-ray source operating at a power of 180 W (15 kV×12 mA) and a hemispherical analyser in fixed analyser transmission mode. High-resolution spectra were recorded at a pass energy of 40 eV with an overall spectral resolution of better than 0.9 eV.

Optical microscopy. Optical microscopic images were collected using a Nikon ECLIPSE LV100 optical microscope.

Confocal microscopy. Confocal microscopic measurements were performed on an inverted microscope (Olympus IX71) with confocal scanning unit (FV300). A cavity dumped mode-locked titanium sapphire laser (Coherent Mira/APE PulseSwitch, 2.7 MHz), frequency doubled to produce pulses centred at 400 nm, was used as the excitation light source. Pulses were delivered to the input of the confocal scanning unit by a single-mode optical fibre. Emission spectra were recorded using an Ocean Optics fibre spectrometer coupled to output of the modified confocal scanning unit.

Widefield microscopy. Widefield microscopic measurements were performed using the halogen transmission lamp on an inverted microscope (Olympus IX71). The lamp was spectrally filtered to provide 0.005 W cm^{-2} of continuous excitation between 400 – 450 nm, providing illumination of the entire single crystal. The microscope was modified to allow the

widefield emission image to be acquired on a CCD camera (Princeton Instruments CoolSNAP) attached to a side port. Spectrally resolved emission images were acquired through the use of a tuneable bandpass filter device (Thorlabs Kurios WB1, fixed bandwidth of 30 nm FWHM) placed between the microscope and the CCD camera. For the carrier gradient and PHM stability measurements (Fig. 3 and Fig. 4), a 532 nm CW laser beam was focused at the centre of the microplatelets with an elliptical shaped focal spot. This was achieved by introducing an asymmetric angular dispersion onto the 532 nm laser beam with a long focal-length cylindrical lens. Both the 532 nm laser and the 400 nm confocal scanning laser passed through the same 1.4 NA 100x oil-immersion lens used to image the samples.

Theoretical Simulation. Simulations of photoinduced halide migration within a single crystal were performed using a Kawasaki lattice model[41]. The halide ions were represented as nodes on a square 2D lattice, where each node can assume values of ±1. In the model, a +1 node corresponds to an I^- ion and a -1 node to a Br^- ion. Unlike the classical Ising model[42], the total number of +1 and -1 nodes is conserved as halide exchanges are only allowed between two nodes of opposite sign. Furthermore, the exchange is allowed between neighbouring nodes only. A Monte Carlo (MC) algorithm was used to solve for the time evolution. The locality of the exchange, together with its known rate, allows the simulation to resemble an actual phase space trajectory as the system approaches equilibrium. This algorithm is therefore similar to a Kinetic MC one[43], but with only one possible transition rate for the halide hopping/exchange.

The time for vacancy mediated halide hopping in perovskites can be calculated from the associated activation energy and lattice vibration frequency[7, 33]. For $MAPbI_3$ in the dark, the I- hopping rate corresponds to roughly 1 ms and, given that the I- ion is the slowest diffusing halide, this is the real time that we assign to 1 MC cycle. There is, however, evidence that the halide hopping rate is faster under illumination[34]. Using this, the simulation results presented in this work correspond to a total time of 0.5 s. Vacancies are not explicitly considered. Also,

only the effects of the CW laser are examined. This is because, for the CW laser, a steady carrier density is established within 1 us of light exposure (see Supplementary Fig. 20), well within the 1ms represented by a single MC step. For the pulsed laser however, the carrier density never reaches a steady state, but fluctuates over periods of 370 ns.

Assuming an average halide-halide distance of ~5 Å along a planar slice of the perovskite cubic phase, the simulated region corresponds to a crystal size of 0.5 µm ×2 µm (i.e. 1000×4000 lattice sites). The similarity between the experimental and simulation results indicates that our 2D model provides an adequate description of the dominant driving forces in the experiments. This is likely due to the high absorption coefficient of perovskite crystals[44], which limits the laser penetration depth for lasers <530 nm (the case in our experiments) to 100-200 nm.

The Hamiltonian of the system is

$$H = -J\Sigma_{(i,j)^{2nd}}\sigma_i\sigma_j - \Sigma_i h_i\sigma_i$$

where J is the interaction strength of the system between adjacent nodes (i, j) and is representative of the free energy of halides mixing. In our model, $J = -1$ for the first four neighbour nodes and $J = -1/2$ for the second four neighbour nodes. This ensures that in the dark the equilibrium of the halide distribution is homogeneous even for a crystal with only 20% I^- (as configurations where an I^- has 8 Br^- on bordering nodes are energetically favoured).

The initial distribution of halides on the lattice was chosen at random to resemble the natural occurring fluctuations of as-grown crystals. We note, however, that a uniform halide distribution has no noticeable effect on the simulation results except for the first few MC cycles (see Supplementary Fig. S16). This is consistent with experimental data[45], which show the degree of homogeneity only affecting the first 10 to 20 seconds of segregation dynamics upon light exposure.

The external field h_i represents the coupling strength of halides with the polaron field at different locations in the lattice. A single polaron is modelled as a gaussian distribution with

a standard deviation $\sigma \approx 3$ lattice nodes[27, 28, 29]. No distinction is made between electron or hole polarons. The effect of h_i is that of attracting I^- ions towards the centre of a polaron favouring any exchange that results in I^- getting closer (Br^- further away) according to the mechanism proposed by Bischak *et al.*[13] (phase segregation driven by localised lattice strain associated with the presence of an excited electron, i.e. polaron).

The Metropolis acceptance probability is

$$e^{-\frac{(\Delta H_{ij}+E_b)}{k_B T i}}$$

where ΔH_{ij} is the energy difference between configurations before and after swapping halides across nodes $i \leftrightarrow j$, E_b is the activation energy due to halide hopping and T_i is the local temperature at node i which increases if polarons are present, i.e. $T_i = T_i(h_i)$, due to carrier thermalization[46].

T_i, E_b and h_i are expressed in the same units as J. In this model $E_b = 1$; the maximum intensity of the polaron field (i.e. the height of the gaussian distribution peak) is $h_i^{max} = 15$; the minimum temperature in the absence of light is $T_i^{min} = 0.5$ while $0.5 < T_i < 2.5$ under laser illumination, i.e. if polarons are present at the lattice location. This temperature range does not reflect a specific real temperature variation across the crystal but was instead tuned (along with the other energy parameters) to accelerate the dynamics of the halides in response to laser excitation, as the accessible simulation time is considerably shorter than that of the experiments. In the absence of the polaron field, our model remains well-mixed at all temperatures, consistent with similar Kawasaki lattice models [47].

It is important to note that, in the model as in experiments, temperature is not what stabilises the remixed state. The temperature only affects the halide kinetics locally during PHS but is never high enough to entropically drive remixing. To confirm this, we performed simulations using a constant temperature across the whole lattice, irrespective of the presence of polarons. No changes were found in the halide distributions in the steady state, during both

low and high intensity light exposures (Supplementary Fig. 19). This is consistent with the experimental data reported in this manuscript (Supplementary Fig. 17) and the literature[37].

For a low intensity laser at 400 nm and 0.1 W cm^{-2}, the number of photons is ~2x10^6 photons/μm^2/ms, which, using an absorbance of $\alpha=10^{-5}$ cm^{-1}, corresponds to ~2x10^7 carriers/μm^3/ms. As the lattice is 2D, we consider the number of carriers in a slab 1nm thick, i.e. ~2x10^4 carriers/ms. For simulations at low power, and at medium to high powers in Fig. S18, we used polaron numbers of 2.8×10^4, 4×10^5 and 2×10^6 respectively. The number for the low power case is within the range of values found in the literature[6, 48].

During most of our simulations, the carrier dynamics was treated statistically. This includes all of the uniform intensity results shown in Supplementary Fig. 18. This is due to the diffusion rate of carriers/polarons ($D_{e/h}$ ~10^{-6} cm^2 s^{-1}), which is orders of magnitude higher than that of ions (D_{ion} ~10^{-12} cm^2 s^{-1}) [29, 33]. For every MC cycle the polarons' location on the lattice is updated according to a probability distribution which preferentially biases the polarons to be on nodes with higher local concentration of I^- (linearly with respect to the concentration, see Supplementary Fig. 20). This is in order to account for the bandgap funnelling effect which drives carriers to regions of lower bandgap. The diffusion length of carriers in perovskites is >3 μm [48] and this, together with a high diffusion rate, means that for every MC cycle their location can be treated independently of their previous position.

As the model cannot account for the carrier diffusion which would take place away from a region at high laser intensity, the simulations in the presence of the green laser shown in Fig. 3 were obtained using a static polaron field for the spot illuminated by the green laser (10 W cm^{-2}) and its adjacent areas. The central region, being saturated with carriers, had the field h_i equal to its maximum value (h_i^{max}) at every lattice node. Away from this spot, the carrier density is expected to decrease smoothly as in drift-diffusion models of carriers in solar cells[49] , and accordingly the field h_i was given the shape of percolating domains of decreasing

connectivity (as previously calculated from simulations performed on lattices uniformly subjected to different fluences, see for example Supplementary Fig. 18).

Spectroscopic images, i.e. widefield and confocal measurements, were generated from the matrix containing the halide ions values (σ_i) on the 2D lattice, weighted by the matrix of the polaron field (h_i). Matrix h_i represents the photoemission intensity (proportional to the carrier/polaron density), while from σ_i we have knowledge of the local halide composition and, consequently, the wavelength of the emitted light. Before and after performing the weighting, Gaussian filters with kernel standard deviations between $20<\sigma<50$ nodes are applied to the matrices. Smoothing is required in order to evaluate the bandgap at each node (i.e. the halide density in a circular region centred at the node) and to account for the limited optical resolution of the instruments.

Data availability

The data that support the findings of this study are available from the corresponding authors on reasonable request.

References

41 Kawasaki, K. In Phase Transitions and critical phenomena, ed. by C. Domb, M.S. Green, Vol. 2 (Academic, New York 1972) p. 443. (1972).

42 Ising, E. Beitrag zur theorie des ferromagnetismus. *Z. Phys.* **31**, 253-258 (1925).

43 Voter, A. F. “Introduction to the kinetic monte carlo method, in radiation effects in solids” in *Radiation Effects in Solids* 1-23 (Springer Netherlands).

44 Yin, W.-J., Shi, T. & Yan, Y. Unique properties of halide perovskites as possible origins of the superior solar cell performance. *Adv. Mater.* **26**, 4653-4658 (2014).

45 Suchan, K., Merdasa, A., Rehermann, C., Unger, E. L., Scheblykin, I. G. Complex evolution of photoluminescence during phase segregation of $MAPb(I_{1-x}Br_x)_3$ mixed halide perovskite. *J. Lumin.* **221**, 117073 (2020).

46 Frost, J. M., Whalley, L. D. & Walsh, A. Slow cooling of hot polarons in halide perovskite solar cells. *ACS Energy Lett.* **2**, 2647-2652 (2017).

47 Das, P., Saha-Dasgupta, T. & Puri, S. Universality of domain growth in antiferromagnets with spin-exchange kinetics. *Eur. Phys. J. E* **40**, 94 (2017)

48 Johnston, M. B. & Herz, L. M. Hybrid perovskites for photovoltaics: charge-carrier recombination, diffusion, and radiative efficiencies. *Acc. Chem.* **49**, 146-154 (2016).

49 Mikhnenko, O. V., Blom, P. W. M. & Nguyen, T.-Q. Exciton diffusion in organic semiconductors. *Energy Environ. Sci.* **8**, 1867-1888 (2015).